

---

Injectable Self-Healing Antibacterial Bioactive Polypeptide-based Hybrid Nanosystems for Efficiently Treating Multidrug Resistant Infection, Skin Tumor Therapy and Enhancing Wound Healing

Li Zhou<sup>a, b</sup>, Yuewei Xi<sup>b</sup>, Yumeng Xue<sup>b</sup>, Min Wang<sup>b</sup>, Yanle Liu<sup>a</sup>, Yi. Guo<sup>b, d</sup>, Bo Lei<sup>a, b, c \*</sup>

<sup>a</sup>Key Laboratory of Shaanxi Province for Craniofacial Precision Medicine Research, College of Stomatology, Xi'an Jiaotong University, Xi'an, 710049, China

<sup>b</sup>Frontier Institute of Science and Technology, Xi'an Jiaotong University, Xi'an, 710049, China

<sup>c</sup>Instrument Analysis Center, Xi'an Jiaotong University, Xi'an, 710049, China

<sup>d</sup>Department of Biomedical Engineering, University of Michigan, Ann Arbor, MI 48109, USA

\* To whom correspondence should be addressed.

Professor Bo Lei, Tel.: +86-29-83395361.

E-mail: rayboo@xjtu.edu.cn

L. Zhou, Y. Liu, Professor B. Lei

Key Laboratory of Shaanxi Province for Craniofacial Precision Medicine Research, College of Stomatology, Xi'an Jiaotong University, Xi'an, 710049, China

This is the author manuscript accepted for publication and has undergone full peer review but has not been through the copyediting, typesetting, pagination and proofreading process, which may lead to differences between this version and the [Version of Record](#). Please cite this article as [doi: 10.1002/advs.11806883](https://doi.org/10.1002/advs.11806883).

This article is protected by copyright. All rights reserved.

---

Email: rayboo@xjtu.edu.cn

L. Zhou, Y. Xi, Y. Xue, M. Wang, Y. Guo, Professor B. Lei

Frontier Institute of Science and Technology, Xi'an Jiaotong University, Xi'an, 710049, China

Professor B. Lei

Instrument Analysis Center, Xi'an Jiaotong University, Xi'an, 710049, China

Y. Guo

Department of Biomedical Engineering, University of Michigan, Ann Arbor, MI 48109, USA

**Abstract:**

The surgical procedure in skin tumor therapy usually results in the cutaneous defects, and multidrug-resistant bacterial infection could cause the chronic wound. Here, for the first time, we developed an injectable self-healing antibacterial bioactive polypeptide-based hybrid nanosystem for treating multidrug resistant infection, skin tumor therapy and wound healing. The multifunctional hydrogel was successfully prepared through incorporating monodispersed polydopamine functionalized bioactive glass nanoparticles (BGN@PDA) into an antibacterial F127- $\epsilon$ -Poly-L-lysine (FEPL) hydrogel. The nanocomposites hydrogel displayed excellent self-healing and injectable as well as robust antibacterial activity especially the multidrug resistant bacterial *in vitro* and *in vivo*. The nanocomposites hydrogel also demonstrated outstanding photothermal performance with (near-infrared laser irradiation) NIR irradiation, which could effectively kill the tumor cell (>90%)

---

inhibit tumor growth (inhibition rate up to 94%) in a subcutaneous skin tumor model. In addition, the nanocomposites hydrogel could effectively accelerate the wound healing *in vivo*. These results that BGN-based nanocomposites hydrogel probably is a promising candidate for skin tumor therapy, wound healing and antiinfection. This work may offer a facile strategy to prepare multifunctional bioactive hydrogels for simultaneous tumor therapy, tissue regeneration and antiinfection.

**Keywords:** Bioactive nanosystems; Multifunctional biomaterials; Tissue engineering; Tumor therapy; Wound healing;

## 1. Introduction

Skin plays an important role in keeping body homeostasis and protecting body from many substance<sup>1</sup>. Skin cancer is diagnosed over a million cases every year, which showed high incidence in western countries<sup>2,3</sup>. The current treatment of skin tumor in clinic mainly includes surgical excision, chemo/radiotherapy and immunotherapy<sup>3-5</sup>. However, many normal skin tissues around the cells must be cleared to prevent recurrence, which results in large skin defects followed by infection chronic wound healing<sup>4</sup>. Additionally, the traditional chemo/radiotherapy has been widely used to avoid recurrence, but the severe side-effect and resistance cause the endless pain to patients<sup>5,6</sup>. Until now, it is a major challenge to fulfill the cancer therapy, wound healing and anti-infection after remove of tumor<sup>7</sup>. Specially, multidrug resistant bacterial infection was one of the key obstacles in chronic wound healing<sup>8</sup>. Therefore, it is significant for designing novel biomaterials for treating

---

accelerating wound healing and multidrug resistant bacterial infection. To the best of our knowledge, there are very few biomaterials with such three functions for efficient skin tumor therapy.

In recent years, photothermal therapy (PTT) has been emerged as a promising strategy to treat various cancers due to the high efficiency and low toxicity<sup>9, 10</sup>. Various photothermal agents have been extensively developed, including many inorganic nanomaterials (gold nanostructures and nanomaterials) and organic PTT agents such as peptide- and protein-based nanomaterials, micelles containing NIR dye, organic/inorganic nanocomposites and conjugated polymers and so on<sup>11-16</sup>. Polydopamine (PDA) has been employed as important biomaterials based on its excellent biocompatibility and lower toxicity *in vitro* and *in vivo*. Specially, PDA could be used for the tumor therapy owing to its good photothermal performance<sup>17-19</sup>. Due to the mussel-inspired characteristic, PDA was easily to be deposited on the surface of nanoparticles. PDA functionalized nanoparticles are also easily to conjugate with other biopolymers through the amidation or Schiff base reaction with PDA. Then the uniform nanocomposites with multifunctional properties could be fabricated *via* the PDA-based chemistry<sup>18, 20, 21</sup>. The multifunctional hybrid hydrogel based on PDA was also reported various biomedical applications<sup>22-24</sup>.

Silicon-based bioactive biomaterials such as bioactive glass (BG, typical composition:  $\text{SiO}_2\text{-CaO-P}_2\text{O}_5$ ), have been extensively used for bone tissue repair, owing to its good biodegradation, tissue regeneration ability<sup>25-34</sup>. Monodispersed BG nanoparticles (BGNs) with enhanced biological performance were also developed for bioimaging, osteogenic differentiation of

---

stem cells, drugs and gene delivery<sup>32-38</sup>. Recently, it was shown that nanoscale BG could enhance chronic wound healing through improving the angiogenesis<sup>38, 39</sup>. Thus various biodegradable nanocomposites based on BGNs were fabricated to meet the increased requirement of tissue repair regeneration<sup>40, 41</sup>.

Hydrogels based on biodegradable biomaterials have become a promising tool for biomedical application owing to their biomimetic mechanical environment and easily preparation to fit special needs<sup>42-47</sup>. Some multifunctional hydrogels and novel biocompatible polymers have been developed drug delivery, cancer therapy, and bacterial infection and wound healing<sup>48-53</sup>. However, hydrogel with efficient anti-infection ability especially multidrug-resistant antibacterial activity, skin tumor therapy and wound healing are few reported<sup>44</sup>.

Herein, we develop a multifunctional bioactive nanocomposites hydrogel with self-healing and antibacterial capacity against multidrug resistant bacteria for photothermal therapy of skin tumor and wound healing. The multifunctional hydrogel was fabricated through the click chemical crosslinking F127- $\epsilon$ -Poly-L-lysine (FEPL), F127-Phe-CHO and BGN@PDA (FCB hydrogel, F: FEPL; C: F127-Phe-CHO; B: BGN@PDA). In this strategy, BGN@PDA was designed to achieve photothermal effect and stimulate the skin repair. FEPL was used to anti-infection, originating from EPL which showed high antibacterial activity in our previous report<sup>54</sup>, and could form the hydrogel network with F127-Phe-CHO and BGN@PDA through the Schiff base reaction. The synthesis, physicochemical

---

structure and properties, biomedical functions of FCB hydrogel in skin cancer treating, anti-infection and skin repair were totally investigated.

## **2. Experimental section**

### **2.1. Fabrication and characterizations of FCB hydrogel**

Dibenzaldehy determined F127 (F127-Phe-CHO) and F127-EPL (FEPL) copolymer was prepared in a similar method as described previously, as shown in Supporting Information<sup>55, 56</sup>. The FCB hydrogel was prepared through a facile mixing method. Briefly, 20 wt% F127-Phe-CHO aqueous solution, 40 wt % FEPL aqueous solution and 5 wt % BGN@PDA solution aqueous were prepared, respectively. Then, 80  $\mu$ L BGN@PDA solution (0.004 g, 5 wt %) and 70  $\mu$ L F127-Phe-CHO (0.014 g, 20 wt %) solution were added to 250  $\mu$ L FEPL solution (0.1g, 40 wt %) at ice. After vortexing, the mixture was kept at 37°C to form hydrogel. The final volume percentage of FEPL and BGN@PDA were kept 25 wt % and 1 wt %, respectively. Similarly, the hydrogel using 80  $\mu$ L H<sub>2</sub>O instead of BGN@PDA was prepared by the same procedure and used as control, denoted as FCE (F: FEPL; C: F127-Phe-CHO; E: without BGN@PDA). The characterizations procedures of hydrogel were presented in supporting information.

### **2.2. Rheological mechanical properties evaluations**

The rheological property (storage G' and loss modulus G'') of hydrogels were determined by a TA rheometer (DHR-2, USA). The hydrogels were placed between the parallel plates of 20 nm

---

diameter and with a gap of 1000  $\mu\text{m}$ . The temperature effect of various hydrogels in the range of 10-37.5°C was evaluated by keeping the strain and frequency constant at 1% and 1 Hz, respectively. The  $G'$  and  $G''$  of hydrogels at 25°C or 37°C were also recorded. The shear-thinning analysis was carried out through changing the strain (from 1% to 1000% with 100 s interval) for three cycles. The time sweeps were used to indicate the change of  $G'$  and  $G''$  were recorded by time sweeps with fixed temperature (25°C) and frequency (1 Hz).

### **2.3. Multifunctional performance evaluations**

The self-healing behavior for hydrogels was measured by macroscopic self-healing experiment. Briefly, the FCB hydrogel was made into 24-well plates (15 mm diameter, 3 mm thickness) with a cavity (4 mm diameter, 3 mm thickness) and placed for 6-12 h (25°C). The self-healing behavior of FCB hydrogel was taken by digital photographs. The followed procedure was used to determine the injectable ability of FCB hydrogel. 400  $\mu\text{L}$  FCB hydrogel was prepared in a 1 mL syringe as described above. The gel was extruded through syringe without clogging, once the solution turned into gel state.

The photothermal effects of the FCB hydrogel, FCE and  $\text{H}_2\text{O}$  were determined in a 24-well culture plate upon irradiation by a laser (808 nm,  $1.41 \text{ W}\cdot\text{cm}^{-2}$ , 10 min). FCB without irradiation was used as control. The temperature growth curves and thermal imaging was analyzed through a machine (Fluke VT04A Visual IR Thermometer) in real time.

### **2.4. *In vitro* photothermal therapy and cytotoxicity assay**

---

A375 cells were firstly cultured under a standard incubation condition (8000/well, DMEM with 10% FBS). After 24 h, the culture solution was changed to be 100  $\mu\text{L}$  fresh medium with FCB hydrogel (8  $\mu\text{L}$ , 0.2  $\mu\text{g}/\mu\text{L}$  FEPL, 0.032  $\mu\text{g}/\mu\text{L}$  F127-Phe-CHO, 0.08  $\mu\text{g}/\mu\text{L}$  BGN@PDA). The cells were irradiated by a NIR laser for 10 min (808 nm, 1.41  $\text{W}\cdot\text{cm}^{-2}$ ). As controls, cells with FCE and blank were treated with or without laser. The medium was removed after 24 h and the cell was washed with PBS for one time. Then, the cells activity was measured through a Live-dead kit based on the manufacture's protocol and observed by fluorescence microscope (IX53, Olympus, Japan). As the cell viability on laser treatment, FCB hydrogel treated cells were incubated for 24 h after NIR illumination (808 nm, 1.41  $\text{W}\cdot\text{cm}^{-2}$  for various times). Cells were grown without FCB or with FCB under the same conditions with or without irradiation were used as controls. The cell viability was quantified by Alamar Blue<sup>®</sup> kit as described previously<sup>57</sup>. To investigate the cytotoxicity of FCB hydrogel and each component, A375 and C2C12 cells was employed and the experimental procedure was the same as those described above.

## 2.5. Antibacterial performance determination

The antibacterial performance of various samples was tested through several representative bacteria including *S. aureus* (Gram-positive), methicillin-resistant *Staphylococcus aureus* (*MRSA*) and *E. coli* (Gram-negative) as reported previously<sup>58</sup>. The *in vivo* antibacterial test was performed on a *MRSA*-infected mouse model. The detailed procedure was shown in Supporting Information.

## 2.6. *In vivo* photothermal tumor therapy

---

The subcutaneous melanoma tumor model was employed to analyze the *in vivo* photothermal capacity for cancer therapy. The detailed procedure for tumor building and photothermal treatment with hydrogels was exhibited in supporting information. After photothermal therapy for 18 days, the mice were sacrificed and the tumor tissues were removed. The obtained tumors were captured and weighed. To analyze the tissue toxicity, the tumor was fixed by paraformaldehyde in (4% v/v), evaluated using hematoxylin-eosin (H&E) and TUNEL analysis. All sections were observed using a light microscope (BX53, Olympus, Japan).

### **2.7. *In vivo* wound healing**

The wound healing test of FCB hydrogel *in vivo* was carried out by a full-thickness cutaneous wound model. Briefly, the female mice (four-week old, 25-30 g) were anesthetized, then a rounded full thickness wound (diameter: 10 mm) was created on the back after shaved. The mice were randomized into four groups (n = 5) as follows: a control group (Blank), FCB group, FCE group and Tegaderm<sup>3M</sup> group. Then, the wounds were fitted with a FCB or FCE hydrogel (50  $\mu$ L) before coated with hollow Tegaderm<sup>3M</sup>. The mice did not fitted with hydrogel and shielded with or without Tegaderm were used as controls.

Digital photographs of wounds were taken on day 0, 3, 7, 10 and 14, and the wound area was determined by Image-J. The wound size was evaluated as follows: Relative wound area =  $S_t/S_0 \times 100\%$ , where  $S_0$  and  $S_t$  were the wound area on day 0 and on day t (t = 3, 7, 10 and 14), respectively. On 3, 7, 10 and 14 days, specimens of all samples were harvested and stained with H&E and

---

Masson's trichrome based on the manufacture's protocol, respectively. VEGF antibodies were used as the markers of angiogenesis in the wound beds in immunohistochemical staining. Thereafter, the sections were observed by a light microscope (BX53, Olympus, Japan).

### 3. Results and discussion

#### 3.1. Fabrication and characterization of FCB hydrogel

The synthesis process and application in tumor therapy and wound healing of FCB hydrogel are shown in Fig. 1. As shown in Fig. 1A, F127-Phe-CHO and FEPL were synthesized by the reaction of F127-OTs, 4-hydroxybenzaldehyde and EPL, respectively. BGN was decorated with PDA by oxidation and polymerization of DA on its surface<sup>59</sup> (Fig. 1B). FCB hydrogel was performed through a Schiff base process between the amino group of FEPL, the aldehyde group of F127-Phe-CHO and BGN@PDA, respectively. Additionally, it was anticipated that FCB hydrogel has excellent antibacterial ability, effective NIR-induced photothermal tumor therapy and enhanced wound healing ability *in vivo* (Fig. 1C).

The chemical structures of the obtained F127-OTs, F127-Phe-CHO and FEPL were elucidated by <sup>1</sup>H NMR and FTIR (Fig. S1 and Fig. 2). In <sup>1</sup>H NMR spectra, the peaks at  $\delta$  7.91, 7.29 and 2.48 ppm were belonged to the aromatic ring and methyl from TsCl and other strong peak at  $\delta$  1.12 ppm was attributed to the methyl of F127, indicating the formation of F127-OTs (Fig. S1A). The absence of methyl peak (2.48 ppm), new resonance signals of the aromatic ring at  $\delta$  7.81 and 7.01 ppm, aldehyde group at  $\delta$  9.87 ppm, suggested the formation of F127-Phe-CHO (Figs. S1B). In Fig. 2A, the

---

disappearance of proton peaks of aromatic ring and five new proton signals at  $\delta$  3.79, 3.15, 1.79, 1.50 and 1.31 ppm assigned as the methine and methylene groups of EPL, confirmed the formation of FEPL copolymer. The graft ratio of -CHO (~100%) and EPL (~100%) in F127 were calculated according to the integral values of peaks at  $\delta$  1.12 ppm (the methyl of F127),  $\delta$  9.87 ppm (-CHO) and  $\delta$  3.15 ppm (methylene groups of EPL), respectively.

The chemical structures of F127-OTs, F127-Phe-CHO, FEPL, FCE and FCB hydrogel were further confirmed by FTIR (Fig. 2B). The skeletal vibration of aromatic ring of F127-OTs was at  $1600\text{ cm}^{-1}$ . The synthesis of F127-OTs could be confirmed through the peaks at  $2876\text{ cm}^{-1}$  and  $1099\text{ cm}^{-1}$  assigned the C-H/ether stretch bands from F127. The symmetric vibration of carbonyl in aldehyde group of F127-Phe-CHO appeared at  $1687\text{ cm}^{-1}$ . According to the FTIR of the EPL, the absorption of ether bands ( $1099\text{ cm}^{-1}$ ) was expected for F127-OTs. The disappearance of skeletal vibration of aromatic and presence of -NH- stretching band of EPL ( $3247\text{ cm}^{-1}$ ) suggested the formation of FEPL. In the FTIR spectrum of the FCE hydrogels, the disappearance of bands at  $1687\text{ cm}^{-1}$  (aldehyde) and the new peak at  $1662\text{ cm}^{-1}$  (C=N), suggesting the Schiff base reaction between -CHO groups of F127-Phe-CHO and -NH<sub>2</sub> of FEPL<sup>56</sup>.

However, in FCB hydrogel, due to the probable similar crosslinking mechanism between BGN@PDA-F127-Phe-CHO and FEPL-F127-Phe-CHO, therefore, no significant change was observed in the FTIR spectrum of FCE and FCB hydrogel. To demonstrate the interaction between BGN@PDA and F127-Phe-CHO, the XPS analysis was conducted. Additionally, the results of XPS

---

showed that the ratio of oxygen to nitrogen in FCB hydrogel (ca. 2.94, Fig. S2A) was lower than that of in FCE hydrogel (ca. 3.48, Fig. S2B), confirming the interaction between F127-EPL and BGN@PDA in FCB hydrogel, which led to the lower ratio owing to the consumption of oxygen in the reaction. There was no significant difference in crystalline composition between FCB and FCE (Fig. S2C).

The monodispersed PDA coated BGNs (BGN@PDA) were synthesized (shown in SI) and confirmed by UV-Vis-NIR and TEM analysis. UV-Vis spectra displayed an absorption peak at ~415 nm, belonging to PDA (Fig. S1C). The BGN@PDA showed significant near-infrared absorption between 800-1000 nm, predicted its potential photothermal property (Fig. S1C). BGN displayed monodispersed mesoporous nanostructure (~300 nm in diameter) (Fig. S1D). Additionally, BGN@PDA showed that a continuous and smooth membrane with a thickness of ~20 nm was coated on the surface of the BGN, indicating the formation of a layer of PDA film (Fig. S1D). After freeze-drying, FCE and FCB hydrogel showed representative porous structures. By comparison with the image of FCE, some BGN@PDA particles could be found in the image of FCB (Fig. 2C). Additionally, the characteristic peaks of Si in the EDS spectrum of FCB hydrogel further confirmed the existence of BGN@PDA in the obtained hydrogels (Fig. 2D).

### **3.2. Rheological, self-healing and injectable properties**

The sol-gel transformation temperatures in hydrogels were important for the biomedical applications including tumor therapy and wound healing<sup>60, 61</sup>. To evaluate the gelation temperature of

---

the FCE and FCB hydrogels, dynamic temperature sweep rheological experiments were conducted to monitor the gelation process. The storage modulus ( $G'$ ) values in FCB and FCE were greater than the loss modulus ( $G''$ ) when the temperature was more than 30°C, indicating the formation of hydrogels (Fig. S3). The crossover of modulus ( $G'$  and  $G''$ ) of FCB was about 27.8°C, which was lower than that of FCE (about 30.5°C), suggesting that the BGN@PDA could contribute to the formation of hydrogels by the reaction of PDA and  $-NH_2$  of FEPL as described in Fig. 1. At 25°C, the  $G''$  of FCB was higher than that of  $G'$ , indicating its solution state (Fig. 3A). When the temperature reached 37°C, FCB became to gel state (approximately 55 s) (Fig. 3C) owing to the fact of  $G' > G''$ , suggested the temperature-responsive property of FCB hydrogel (Fig. 3A and Fig. 3C). Moreover, the  $G'$  and  $G''$  of FCB were higher than that of FCE at 37°C, further confirming the synergies of BGN@PDA in the formation of FCB hydrogel networks (Fig. S3). The shear-thinning behavior of FCB hydrogel was confirmed by the rheological analysis under high and low shear strain (Fig. 3B). The network of the FCB hydrogels were disrupted by the high shear strain (1000%), resulting in a significant decrease in  $G'$  to a level below  $G''$ . At the low shear strain (1%), the  $G'$  for FCB hydrogels were completely recovered immediately (Fig. 3B), even after three cycles, demonstrating their rapid self-healing and shear-thinning capacity. The self-healing ability of FCB hydrogel was also showed through morphological repair experiment in which a cavity created in hydrogel. After 6 h, the cavity of hydrogel became smaller and disappeared completely after 12 h, indicating the good self-healing capability of FCB hydrogel (Fig. 3D). In addition, the shear-thinning behavior and the excellent

---

self-healing of FCB hydrogel enabled the facile injection capacity without clogging and writing smoothly (Fig. 3E).

### 3.3. Photothermal properties and cytotoxicity evaluation of FCB hydrogel

The temperature changes ( $\Delta_t$ ) of FCB hydrogel was promoted dramatically up to about 40 °C during 9 min (Figs. 4A-B). By contrast, the FCE hydrogel and H<sub>2</sub>O indicated poor temperature changes at the same conditions. FCB hydrogel without NIR irradiation showed no changes in temperature and thermal image. These results displayed that the excellent photothermal performance of FCB hydrogel was due to the incorporation of BGN@PDA. The anticancer efficiency of FCB hydrogel *in vitro* was evaluated in A375 cancer cells. The Live/dead images of cells showed that a large number of dead cells (red fluorescence) were observed in FCB+NIR group (Fig. 4C). By comparison, the cells in the other five groups were almost alive (green fluorescence) (Fig. 4C). The cell viability in FCB + NIR group (10 min) was decreased to 18%, significantly lower than that of controls (NC, FCB and NC+ NIR group) (Fig. 4D). The cell viability of FCB + NIR was further decreased with the increasing of irradiation duration (9.3% for 20 min). Additionally, the cell viability of hydrogels (FCB and FCE) in A375 and C2C12 cells were greater than 80% even incubation for 24 h or 48 h, showing their lower cytotoxicity. These results demonstrated the excellent photothermal therapeutic efficiency of FCB hydrogel with better biocompatibility *in vitro*.

### 3.4. Antibacterial capacity evaluation *in vitro/in vivo*

---

The bacterial infection after surgical tumor therapy has been the one of major obstacles in wounding healing<sup>62,63</sup>, therefore, the antibacterial efficacy of biomaterials is very important. FCB hydrogel exhibited considerable antibacterial-killing ability for *E. coli* and *S. aureus*, which was equivalent to that of FCE (99%), suggesting that BGN@PDA did not affect the antibacterial efficacy of FCB (Figs. 5A-B). In contrast, BGN@PDA and ampicillin showed weak antibacterial activity, in which the highest killing efficiencies were 63% and 56% against *S. aureus*, respectively (Fig. 5B). In addition, FCB hydrogel also showed higher antibacterial activity against *MRSA*, in which the killing efficiency was up to 99%, whereas the corresponding value of ampicillin was 24% (Fig. 5B).

The anti-infection efficacy of FCB hydrogel *in vivo* was also assessed using *MRSA*-infected mouse as the model (Figs. 5C-E). The mice were infected by *MRSA* through subcutaneous injection and were randomly divided into five groups (n = 5) after 3 days infection. The antibacterial efficacy was evaluated by counting the number of bacteria came from the tissue homogenates plated onto LB-agar plates (Figs. 5C and D). Mice treated with ampicillin twice displayed a bacterial with  $2.1 \times 10^7$  CFU mL<sup>-1</sup>, similar with control (PBS-treated group) (Fig. 5D). By comparison, FCB-treated group revealed significant less bacteria, in which the bacteria burden was  $3.75 \times 10^6$  CFU mL<sup>-1</sup>. Additionally, the antibacterial efficacy of FCB (~84%) was significantly higher than that of FCE (~78%) and BGN@PDA (~51%), suggesting that FCB displayed higher antibacterial activity with synergistic effect of FCE and BGN@PDA (Figs. 5C and D). As depicted in Fig. 5E, the inflammatory exudates and the macrophages in the tissue treated by FCB hydrogel was much less than others, demonstrating that the *MRSA* infection *in vivo* was significantly reduced. The antibacterial

---

performance of FCB hydrogel was probably originated from EPL which showed high antimicrobial ability against various bacterial<sup>58, 64</sup>.

### 3.5. *In vivo* antitumor effect of FCB hydrogel

The antitumor efficacy of FCB hydrogel was further confirmed in nude mice with A375 tumor xenografts. After irradiation for 10 min on tumor with various groups, the temperature change ( $\Delta_t$ ) was approximately 5 °C for PBS+NIR group and FCE + NIR groups, and FCB+NIR group showed the rapid improvement for  $\Delta_t$  (16 °C) (the temperature of tumor was about 51 °C) (Figs. 6A-B). The tumor volume of FCB+NIR group was reduced significantly after photothermal therapy for 4 days, while the control groups presented a rapid tumor growth (Figs. 6C-D). The tumor volume in FCB+NIR group was far lower than other three controls, which was reduced by 94% compared to PBS on day 18 (Figs. 6C-D). Additionally, the tumors of FCB + NIR group were gradually disappeared without recurrence after treatments (day 18) (Fig. S4). By comparison, FCB without NIR irradiation had no effect on tumor inhibition, which showed the comparable tumor volume with PBS+NIR and FCE+NIR groups (Figs. 6C-D). Moreover, after 18 days treatment, the mean tumor weight in FCB+NIR group was the smallest among all groups, indicating that FCB hydrogel with NIR efficiently suppressed tumor growth (Fig. 6E).

H&E and TUNEL staining were used to evaluate the microscopic therapeutic efficacy of FCB hydrogel *in vivo*. A lot of apoptotic tumor cells were seen in FCB+NIR group, while cells in controls were well alive (Figs. 6F). In addition, TUNEL<sup>+</sup> apoptotic tumor cells of the FCB+NIR group was

---

much more than other groups as shown in quantitative analysis (Fig. 6G). These results indicated that FCB hydrogel could significantly inhibit tumor development by promoting apoptosis of cancer cells *in vivo* owing to its NIR-induced hyperthermia.

### **3.6. *In vivo* wound healing of FCB hydrogel**

The potential wound healing efficacy of FCB hydrogel was further performed in mice with full-thickness skin wound, using FCE and commercial dressing (3M) as controls. FCB hydrogels presented a higher wound healing rate relative to other groups (\* $p < 0.05$ ) (Figure 7). As compared to FCE and 3M group, on day 3 after surgery, the wound area of FCB group was slightly reduced and the elevated re-epithelialization was obviously detected (Figs. 7A-B). The relative wound areas on day 7 for the FCB hydrogel, FCE, 3M and Blank was 33.1%, 53.5%, 77.6% and 52.5%, respectively (Fig. 7B). The wound defects filled with FCB were almost healed on day 10, in which the relative wound area was 8.3%, by comparison, 29.2%, 40.7% and 31.8% for FCE, 3M and Blank groups, respectively. The remaining wound area on day 14 for FCB (1.2%) was much lower than FCE (4.3%), 3M (24.5%) and Blank groups (13.4%), demonstrating that the wound was almost completely healed (Figs. 7A-B).

Additionally, the H&E images showed that the epidermis of FCB group was gradually appeared with the increasing of time (Fig. S5). On day 14, relative to other groups, abundant granulation tissue (black arrows) was observed in FCB group (Fig. 7C). Granulation tissue included extracellular matrix, fibroblasts and many growth factors, which was beneficial for wound healing process. The

---

granulation tissue thickness in FCB hydrogel group displayed approximately 240  $\mu\text{m}$  thicker than controls (Fig. S5B). Masson's trichrome staining indicated that more positive staining could be observed in FCB group (Fig.S6B), suggesting more collagen content in FCB group (Fig. 7C and Fig. S6). Additionally, the immunohistochemical staining of VEGF expression was also performed to analyze the angiogenesis in wound healing. There were more VEGF positive vessels (brown, black arrows showed) observed in the FCB group than the controls (Fig.S7A), and the quantitative analysis also confirmed the formation of abundant vessels in FCB group (Fig.S7B). These results indicated that FCB hydrogel enhanced wound healing by promoting the thickness of granulation tissue, collagen deposition and angiogenesis. The antibacterial EPL polypeptide and BGN should be responsible for the good performance of wound healing. Previous studies showed that antibacterial EPL-based polypeptide could significantly promote the formation of collagen tissue and angiogenesis, and the BGN could enhance the formation of blood vessel through activating the hypoxia inducible factor (HIF)<sup>8, 38, 39, 52</sup>. Thus, the FCB hydrogel demonstrated the excellent wound healing performance. These results further indicated that FCB hydrogel was probably a versatile biomaterial for treating infection, cancer and tissue injury.

As compared to previous multifunctional biomedical hydrogel, the as-prepared FCB hydrogel possesses several advantages in wound healing. Firstly, FCB hydrogel demonstrated the intrinsic multifunctional capacities including treating multidrug-resistant bacterial infection, inhibiting tumor growth and enhancing wound healing. These three biomedical functions of FCB hydrogel were few reported for previous biodegradable hydrogels, although the wound healing/antiinfection/antitumor

---

after tumor surgery were rather necessary in helping the recovery of patients. Additionally, the components in FCB hydrogel including EPL, F127 and BGN have shown high biosafety, and the synthesis is facile and suitable for large-scale production. Compared with other antibacterial agents including metal ions and polymer, as a natural polypeptide, EPL has the high biocompatibility and excellent broad-spectrum activity including multidrug-resistant bacteria<sup>8, 54, 63, 64</sup>. EPL-based polymers also demonstrated promising applications in tissue regeneration and gene therapy<sup>8, 63</sup>. This study provided a facile strategy to construct a bioactive polypeptide-based hydrogel with multifunctional properties for integrated disease therapy-tissue regeneration.

#### 4. Conclusions

In summary, a self-healing, injectable and antibacterial bioactive polypeptide-based nanocomposites hydrogel was developed for anti-infection, skin cancer therapy and skin repair *in vitro* and *in vivo*. FCB hydrogel showed good self-healing and shear-thinning behavior with good injectable capacity. FCB hydrogel possessed rapid photothermal performance with effectively killing cancer cells *in vitro* with negligible cytotoxicity. Additionally, FCB hydrogel demonstrated high antibacterial capability toward *E. coli*, *S. aureus* and *MRSA* *in vitro* and *in vivo*. Importantly, FCB hydrogel could significantly suppress the tumor growth and ablate tumor *in vivo* through efficient photothermal response. FCB hydrogel could also effectively promote the wound healing *in vivo* via stimulating the formation of collagen and angiogenesis. This work demonstrates that FCB hydrogel is a promising candidate for antiinfection, tumor therapy and wound healing. Additionally, the strategy

---

described in this work could be used to prepare other novel hydrogels for multifunctional cancer therapy and tissue regeneration.

### Acknowledgments

This work was supported by National Natural Science Foundation of China (Grant No.51872224), Key Laboratory of Shaanxi Province for Craniofacial Precision Medicine Research, College of Stomatology, Xi'an Jiaotong University (Grant No. 2018LHM-KFKT004), the Joint Funds of the National Natural Science Foundation of China (Grant no. U1501245).

### Reference

- [1]. D. J. Tobin. *Chem. Soc. Rev.* **2006**, 35, 52.
- [2]. M. C. F. Simões, J. J. S. Sousa, A. A. C. C. Pais, *Cancer Lett.* **2015**, 357, 8.
- [3]. K. D. Miller, R. L. Siegel, C. C. Lin, A. B. Mariotto, J. L. Kramer, J. H. Rowland, K. D. Stein, R. Alteri, A. Jemal, *CA Cancer J Clin* **2016**, 66, 271.
- [4]. V. S. C. Pua, S. Huilgol, D. Hill, *Australas. J. of Dermatol.* **2009**, 50, 171.
- [5]. M. Wang, Y. Guo, Y. Xue, W. Niu, M. Chen, P. X. Ma, B. Lei, *Biomaterials* **2019**, 199, 10.
- [6]. A. Stratigos, C. Garbe, C. Lebbe, J. Malvehy, V. del Marmol, H. Pehamberger, K. Peris, J. C. Becker, I. Zalaudek, P. Saiag, M. R. Middleton, L. Bastholt, A. Testori, J. J. Grob, Edf, Eado, Eortc, *Eur. J. Cancer* **2015**, 51, 1989.
- [7]. M. Wu, Y. Xue, N. Li, H. Zhao, B. Lei, M. Wang, J. Wang, M. Luo, C. Zhang, Y. Du, C. Yan, *Angew. Chem. Int. Edit.* **2019**, doi.org/10.1002/ange. 201812972.

- 
- [8]. Y. Xi, J. Ge, Y. Guo, B. Lei, P. X. Ma, *ACS Nano* **2018**, 12, 10772.
- [9]. Y. Li, N. Li, J. Ge, Y. Xue, W. Niu, M. Chen, Y. Du, P. X. Ma, B. Lei, *Biomaterials* **2019**, 201, 68.
- [10]. W. Tao, X. Ji, X. Xu, M. A. Islam, Z. Li, S. Chen, P. E. Saw, H. Zhang, Z. Bharwani, Z. Guo, J. Shi, O. C. Farokhzad, *Angew. Chem. Int. Edit.* **2017**, 56, 11896.
- [11]. Q. Sun, Q. You, X. Pang, X. Tan, J. Wang, L. Liu, F. Guo, F. Tan, N. Li, *Biomaterials* **2017**, 122, 188.
- [12]. M. Abbas, Q. Zou, S. Li, X. Yan, *Adv. Mater.* **2017**, 29, 1605021.
- [13]. J. Li, J. Rao, K. Pu, *Biomaterials* **2018**, 155, 217.
- [14]. M. Aioub, S. R. Panikkanvalappi, M. A. El-Sayed, *ACS Nano* **2017**, 11, 579.
- [15]. X. Song, Q. Chen, Z. Liu, *Nano Res.* **2015**, 8, 340.
- [16]. Y.-W. Chen, Y.-L. Su, S.-H. Hu, S.-Y. Chen, *Adv. Drug Deliver. Rev.* **2016**, 105, 190.
- [17]. Y. L. Liu, K. L. Ai, J. H. Liu, M. Deng, Y. Y. He, L. H. Lu, *Adv. Mater.* **2013**, 25, 1353.
- [18]. L.-S. Lin, Z.-X. Cong, J.-B. Cao, K.-M. Ke, Q.-L. Peng, J. Gao, H.-H. Yang, G. Liu, X. Chen, *ACS Nano* **2014**, 8, 3876.
- [19]. W. Chen, Y. Wang, M. Qin, X. Zhang, Z. Zhang, X. Sun, Z. Gu, *ACS Nano* **2018**, 12, 5995.
- [20]. D. Zhang, M. Wu, Y. Zeng, L. Wu, Q. Wang, X. Han, X. Liu, J. Liu, *ACS Appl. Mater. Interfaces* **2015**, 7, 8176.
- [21]. G. Pan, S. Sun, W. Zhang, R. Zhao, W. Cui, F. He, L. Huang, S.-H. Lee, K. J. Shea, Q. Shi, H. Yang, *J. Am. Chem. Soc.* **2016**, 138, 15078.
- [22]. L. Han, X. Lu, M. Wang, D. Gan, W. Deng, K. Wang, L. Fang, K. Liu, C. W. Chan, Y. Tang, L.-T. Weng, H. Yuan, *Small* **2017**, 13, 1601916.

- 
- [23]. L. Han, X. Lu, K. Liu, K. Wang, L. Fang, L.-T. Weng, H. Zhang, Y. Tang, F. Ren, C. Zhao, G. Sun, R. Liang, Z. Li, *ACS Nano* **2017**, 11, 2561.
- [24]. D. Gan, T. Xu, W. Xing, X. Ge, L. Fang, K. Wang, F. Ren, X. Lu, *Adv. Funct. Mater.* **2019**, 29, 1805964.
- [25]. F. Zhao, B. Lei, X. Li, Y. Mo, R. Wang, D. Chen, X. Chen, *Biomaterials* **2018**, 178, 36.
- [26]. Y. Xue, Y. Du, J. Yan, Z. Liu, P. X. Ma, X. Chen, B. Lei, *J. Mater. Chem. B* **2015**, 3, 3831.
- [27]. V. Miguez-Pacheco, L. L. Hench, A. R. Boccaccini, *Acta Biomater.* **2015**, 13, 1.
- [28]. Y. Guo, Y. Xue, W. Niu, M. Chen, M. Wang, P. X. Ma, B. Lei, *Part.Part. Syst. Char.* **2018**, 35, 1800087.
- [29]. Y. Du, M. Yu, J. Ge, P. X. Ma, X. Chen, B. Lei, *Adv. Funct. Mater.* **2015**, 25, 5016.
- [30]. J. R. Jones, *Acta Biomater.* **2013**, 9, 4457.
- [31]. F. Zhao, W. Xie, W. Zhang, X. Fu, W. Gao, B. Lei, X. Chen, *Adv. Healthcare Mater.* **2018**, 7, 1800361.
- [32]. Y. Li, Y. Guo, W. Niu, M. Chen, Y. Xue, J. Ge, P. X. Ma, B. Lei, *ACS Appl. Mater. Interfaces* **2018**, 10, 17722.
- [33]. M. Yu, Y. Xue, P. X. Ma, C. Mao, B. Lei, *ACS Appl. Mater. Interfaces* **2017**, 9, 8460.
- [34]. Y. Xue, Z. Zhang, W. Niu, M. Chen, M. Wang, Y. Guo, C. Mao, C. Lin, B. Lei, *Part. Part. Syst. Char.* **2019**, 1800507.
- [35]. Y. Xue, Y. Guo, M. Yu, M. Wang, P. X. Ma, B. Lei, *Adv. Healthcare Mater.* **2017**, 6, 1700630.
- [36]. C. Wu, J. Chang, *J. Control. Release* **2014**, 193, 282.
- [37]. F. Li, M. Wang, G. Pi, B. Lei, *J. Biomed. Nanotechnol.* **2018**, 14, 756.

- 
- [38]. W. Gao, W. Jin, Y. Li, L. Wan, C. Wang, C. Lin, X. Chen, B. Lei, C. Mao, *J. Mater. Chem. B* **2017**, *5*, 7285.
- [39]. C. Wang, Q. Wang, W. Gao, Z. Zhang, Y. Lou, H. Jin, X. Chen, B. Lei, H. Xu, C. Mao, *Acta Biomater.* **2018**, *69*, 156.
- [40]. B. Lei, B. Guo, K. J. Rambhia, P. X. Ma, *Front. Med.* **2018**, 1-13.
- [41]. S. Kargozar, M. Mozafari, R. G. Hill, P. B. Milan, M. T. Joghataei, S. Hamzehlou, F. Baino, *Mater. Today-Proceed.* **2018**, *5*, 15532.
- [42]. R. Xing, K. Liu, T. Jiao, N. Zhang, K. Ma, R. Zhang, Q. Zou, G. Ma, X. Yan, *Adv. Mater.* **2016**, *28*, 3669.
- [43]. X. Bai, M. Gao, S. Syed, J. Zhuang, X. Xu, X.-Q. Zhang, *Bioact. Mater.* **2018**, *3*, 401.
- [44]. J. Fu, M. in het Panhuis, *J. Mater. Chem. B* **2019**, DOI: 10.1039/C9TB90023C.
- [45]. R. Li, J. Xu, D. S. H. Wong, J. Li, P. Zhao, L. Bian, *Biomaterials* **2017**, *145*, 33.
46. K. Zhang, Q. Feng, J. Xu, X. Xu, F. Tian, K. W. K. Yeung, L. Bian, *Adv. Funct. Mater.* **2017**, *27*, 1701642.
- [47]. K. Zhang, S. Lin, Q. Feng, C. Dong, Y. Yang, G. Li, L. Bian, *Acta Biomater.* **2017**, *64*, 389.
- [48]. V. Perci, C. Pin-Barre, C. Rivera, C. Pellegrino, J. Laurin, D. Gigmes, T. Trimaille, *Biomacromolecules* **2019**, *20*, 149.
- [49]. Y. Wu, H. Wang, F. Gao, Z. Xu, F. Dai, W. Liu, *Advanced Functional Materials* **2018**, *28*, 1801000.
- [50]. C. Wang, M. Wang, T. Xu, X. Zhang, C. Lin, W. Gao, H. Xu, B. Lei, C. Mao, *Theranostics* **2019**, *9*, 65.

- 
- [51]. J. Ge, K. Liu, W. Niu, M. Chen, M. Wang, Y. Xue, C. Gao, P. X. Ma, B. Lei, *Biomaterials* **2018**, 175, 19.
- [52]. B. Hu, Y. Shen, J. Adamcik, P. Fischer, M. Schneider, M. J. Loessner, R. Mezzenga, *ACS Nano* **2018**, 12, 3385.
- [53]. L. Zhou, X. Qu, Y. Guo, M. Wang, B. Lei, P. X. Ma, *ACS Appl. Mater. Interfaces* **2018**, 10, 4471.
- [54]. L. Zhou, Y. Xi, M. Yu, M. Wang, Y. Guo, P. Li, P. X. Ma, B. Lei, *Acta Biomater.* **2017**, 58, 90.
- [55]. T. Liu, X. Zhang, B. Ke, Y. Wang, X. Wu, G. Jiang, T. Wu, G. Nie, *Mater. Sci. Eng. C* **2016**, 61, 269.
- [56]. X. Yang, G. Liu, L. Peng, J. Guo, L. Tao, J. Yuan, C. Chang, Y. Wei, L. Zhang, *Adv. Funct. Mater.* **2017**, 27, 1703174.
- [57]. L. Zhou, X. Qu, Y. Guo, M. Wang, B. Lei, P. X. Ma, *ACS Appl. Mater. Interfaces* **2018**, 10, 4471.
- [58]. S. R. Deka, A. K. Sharma, P. Kumar, *Curr. Top. Med. Chem.* **2015**, 15, 1179.
- [59]. L. Han, K. Liu, M. Wang, K. Wang, L. Fang, H. Chen, J. Zhou, X. Lu, *Adv. Funct. Mater.* **2018**, 28, 1704195.
- [60]. L. Klouda, *Eur. J. Pharm. Biopharm.* **2015**, 97, 338.
- [61]. K.-Q. Wang, S.-Z. Luo, X.-Y. Zhong, J. Cai, S.-T. Jiang, Z. Zheng, *Food Chem.* **2017**, 214, 393.
- [62]. S. L. Percival, K. E. Hill, D. W. Williams, S. J. Hooper, D. W. Thomas, J. W. Costerton, *Wound Repair Regen.* **2012**, 20, 647.
- [63]. Y. Du, J. Ge, Y. Li, P. X. Ma, B. Lei, *Biomaterials* **2018**, 157, 40.
- [64]. L. Zhou, Y. Xi, M. Chen, W. Niu, M. Wang, P. X. Ma, B. Lei, *Nanoscale* **2018**, 10, 17304.

#### Figure captions

---

**Figure 1. Scheme showing the preparation and application of FCB hydrogel in tumor therapy and**

**wound healing.** (A) The synthesis route of F127-OTs and FEPL; (B) Schematic illustration for the formation of FCB hydrogel and bioapplication.

**Figure 2. Characterization.** (A)  $^1\text{H}$  NMR spectra of FEPL in  $\text{D}_2\text{O}$ ; (B) FTIR of precursors and FCB hydrogel; (C) FESEM images of FCE and FCB hydrogel; (D) EDS spectrum of FCB hydrogel.

**Figure 3.** (A) Rheological analysis of the FCB hydrogels at  $25^\circ\text{C}$  and  $37^\circ\text{C}$ ; (B) Rheological data of FCB hydrogel under alternating high (1000%) and low shear (1%); (C) the images of the FCB hydrogel forming;

(D-E) images of self-healing and injectability of the FCB hydrogels.

**Figure 4. Photothermal performance and *in vitro* anticancer efficiency.** (A-B) The real-time infrared thermal images and photothermal heating curves of FCB hydrogel and controls with NIR irradiation ( $808\text{ nm}$ ,  $1.41\text{ W}\cdot\text{cm}^{-2}$ ); (C) *in vitro* anticancer efficiency of FCB hydrogel and controls with or without NIR treatment ( $808\text{ nm}$ ,  $1.41\text{ W}\cdot\text{cm}^{-2}$ , 10min); (D) FCB hydrogel under different irradiation duration ( $808\text{ nm}$ ,  $1.41\text{ W}\cdot\text{cm}^{-2}$ ) (\* $p < 0.05$ , \*\* $p < 0.01$ , \*\*\* $p < 0.001$ ); (E) the cytotoxicity of FCB hydrogel and each composite in A375 and C2C12 cells.

**Figure 5. Antibacterial activity *in vitro* and *in vivo*.** (A) Pictures of agar plates and (B) corresponding statistical data of colonies densities of *E. coli*, *S. aureus* and *MRSA* treated with different samples (\* $p < 0.05$  and \*\* $p < 0.01$ ). (C) Images of *MRSA* colonies growing on the agar

---

plates come from the homogenized infected tissues after PBS buffer (Control), Ampicillin, BGN@PDA, FCE and FCB treatment; (D) Quantitative bacterial colonies densities based on (C) ( $*p < 0.05$  and  $**p < 0.01$ ); (E) Optical images of H&E stained tissue sections after treated with PBS buffer (Control), Ampicillin, BGN@PDA, FCE and FCB, respectively (scale bars: 50  $\mu\text{m}$ ).

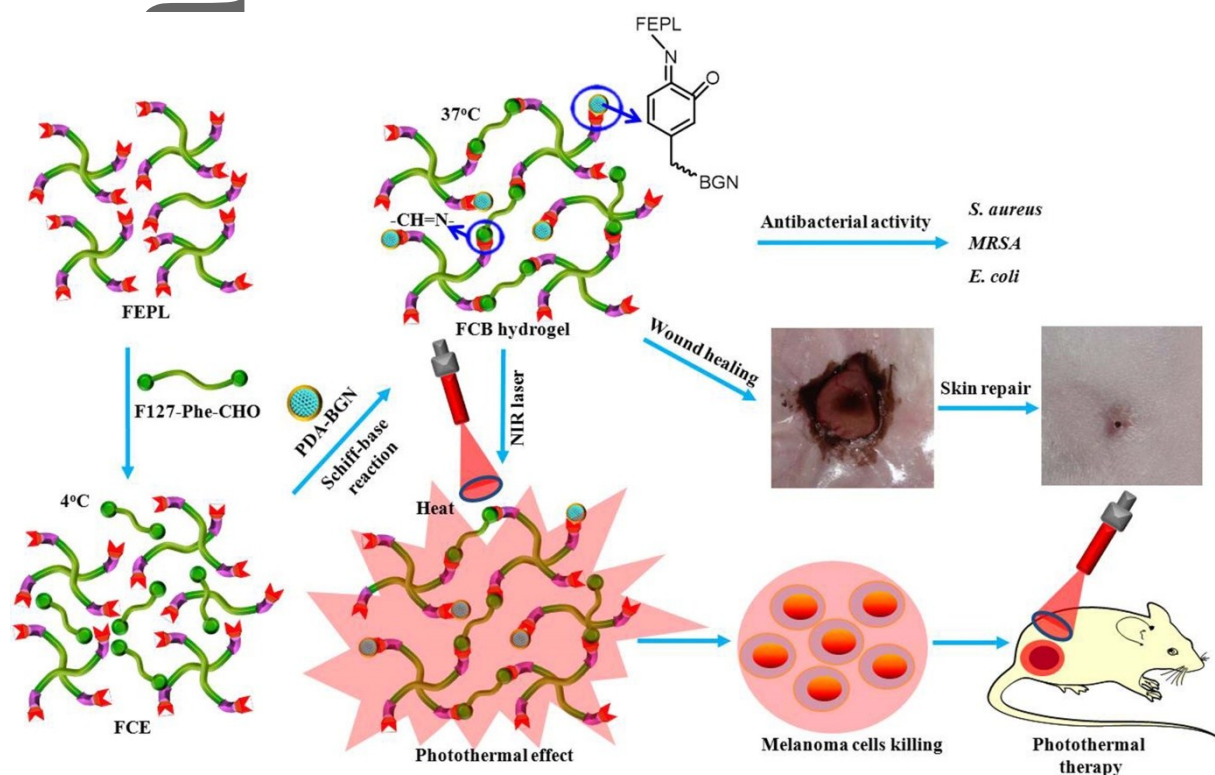
**Figure 6. *In vivo* photothermal therapy of FCB hydrogel.** (A) NIR thermal images of FCB hydrogel and (B) photothermal heating curves of A375 tumor-bearing mice treated with FCB, FCE and PBS when treated with or without irradiation (808 nm,  $1.41 \text{ W} \cdot \text{cm}^{-2}$ , 10 min); (C) photographs of the tumors after various treatments on day 18; (D) Tumor volume and weight (E) at the end of experiment; (F) Images of HE and TUNEL analyses of tumor tissues after treatment for 18 days with various formulations. ( $*p < 0.05$  and  $**p < 0.01$ , Scale bar: 20  $\mu\text{m}$ ); (G) Tunel<sup>+</sup> tumor cells in tumor sections quantified by Image-J.

**Figure 7. *In vivo* wound healing in mice.** (A) Representative skin wound photographs on days 0, 3, 7, 10 and 14 and (B) wound closure rates of the FCB, FCE and controls ( $*p < 0.05$ ,  $**P < 0.01$ ,  $***P < 0.001$ ); (C) H&E and Masson's trichrome staining of wounds after 14 d postsurgery treated with FCB hydrogels and controls, fibrin glue. The black arrows show the granulation layers in wound beds. Scale bar is 100  $\mu\text{m}$ .

## TOC Text

This paper reports an intrinsically multifunctional bioactive hybrid hydrogel for treating multidrug resistant infection, skin tumor therapy and wound healing. The hybrid hydrogel displayed excellent self-healing and injectable ability, as well as robust antibacterial activity especially the multidrug resistant bacterial *in vitro* and *in vivo*, efficient inhibits tumor growth and enhances wound healing.

## Figures



## Graphic abstract

---

# Author Manuscript

This article is protected by copyright. All rights reserved.

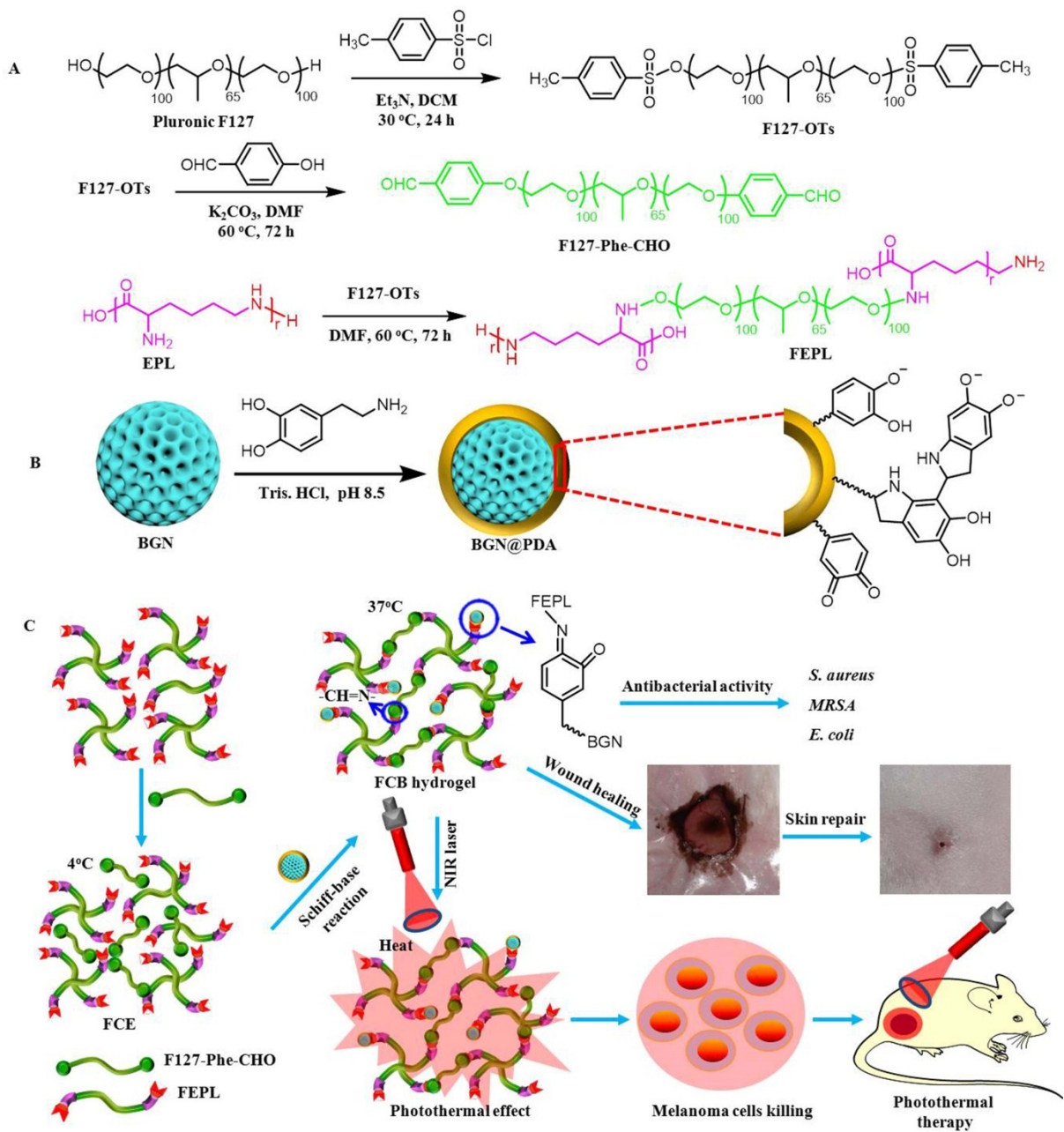


Figure 1

Auth

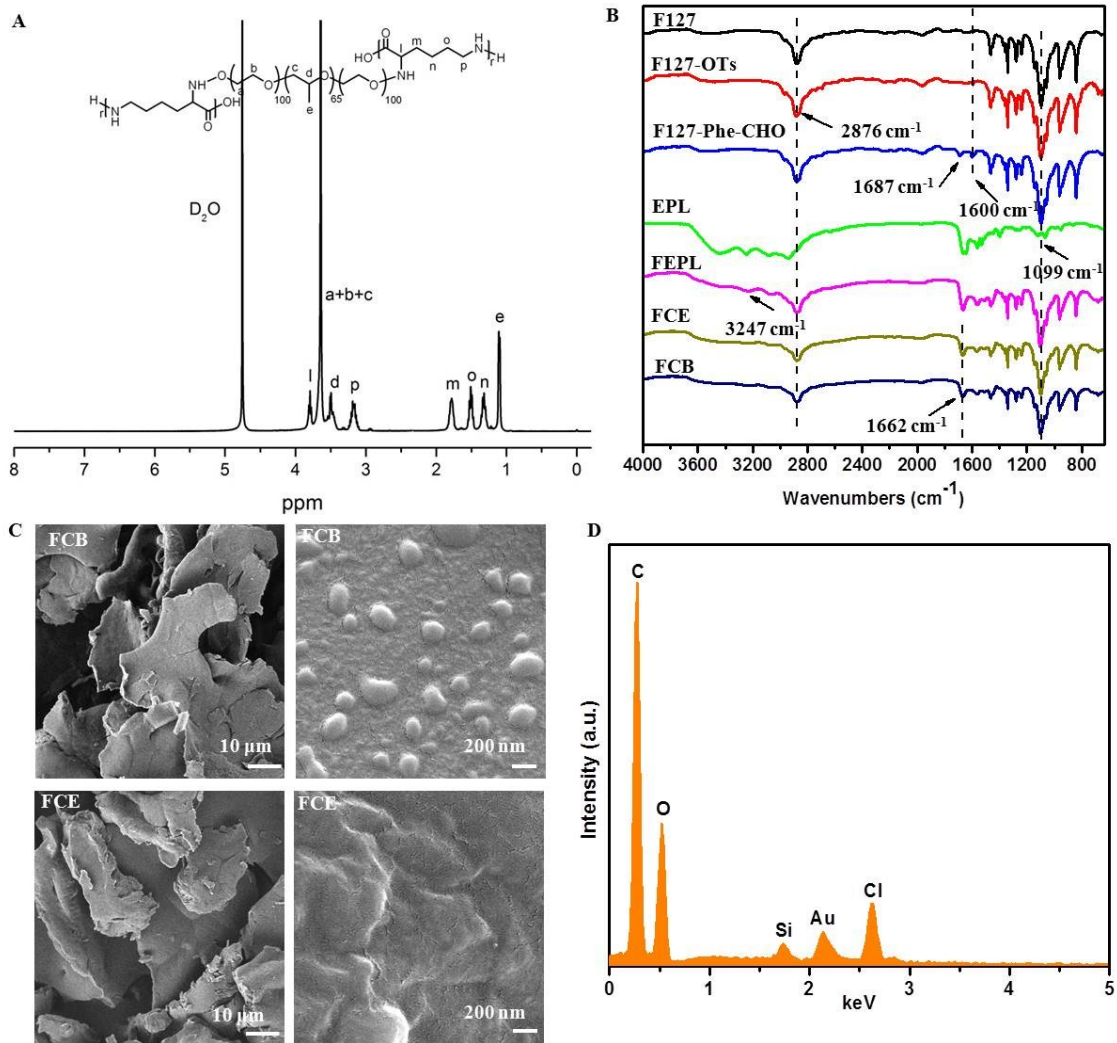


Figure 2

Author

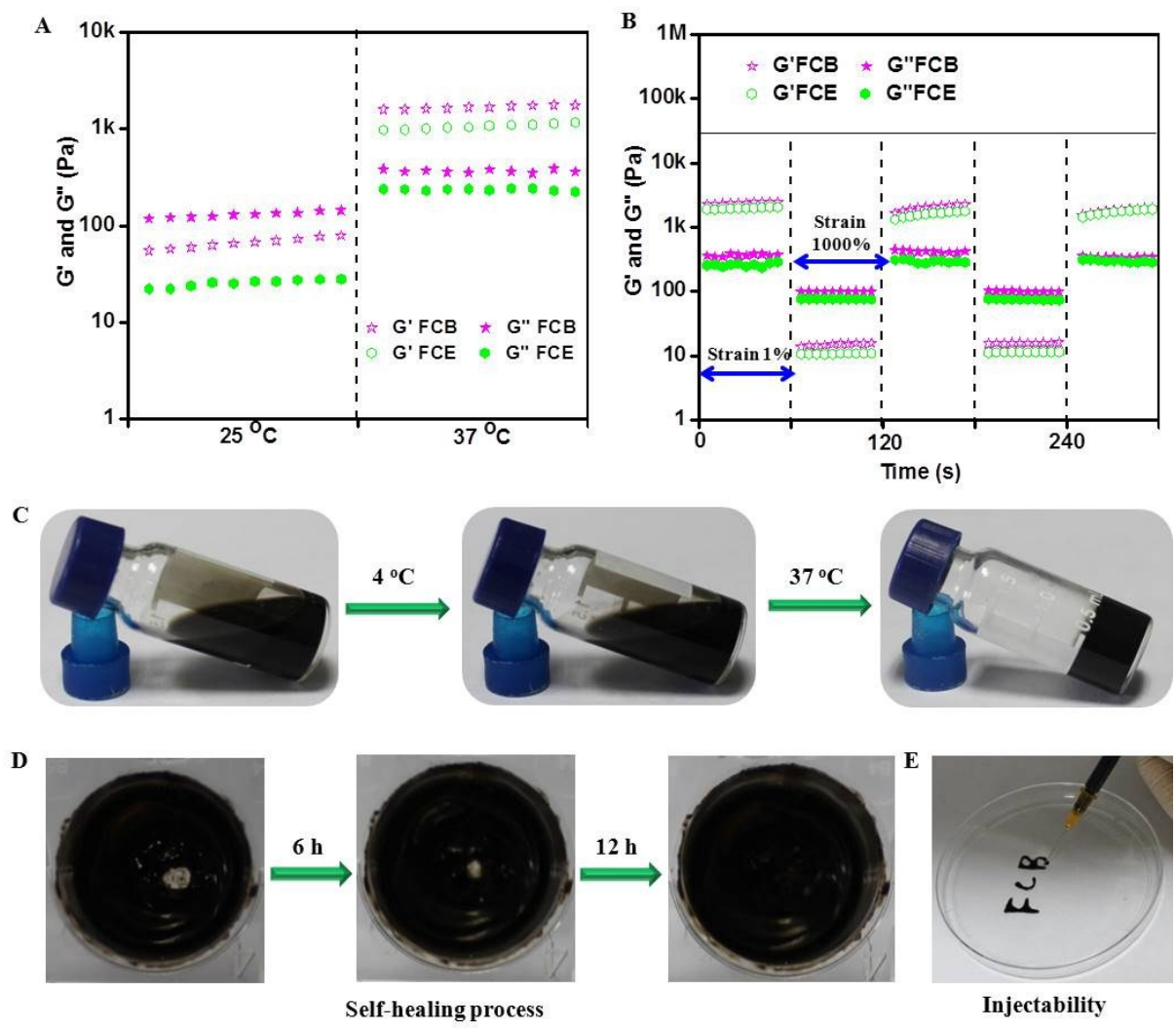


Figure 3

Author

ot

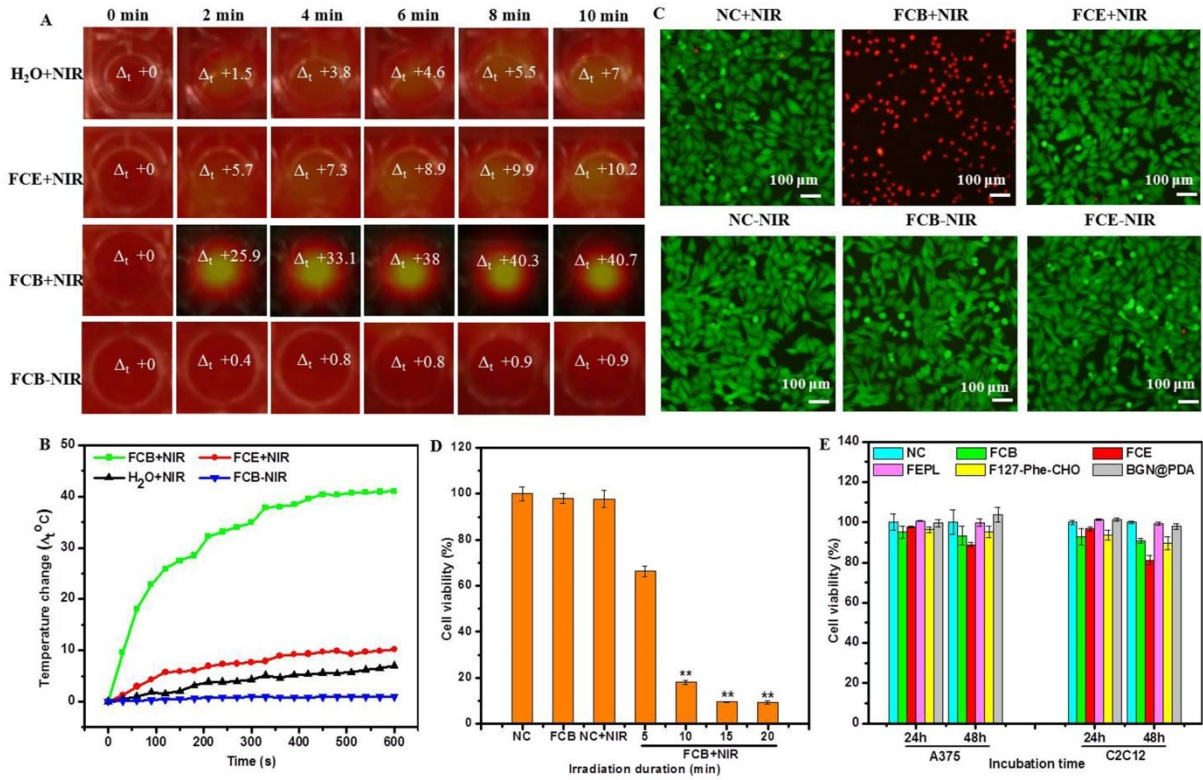


Figure 4

Author

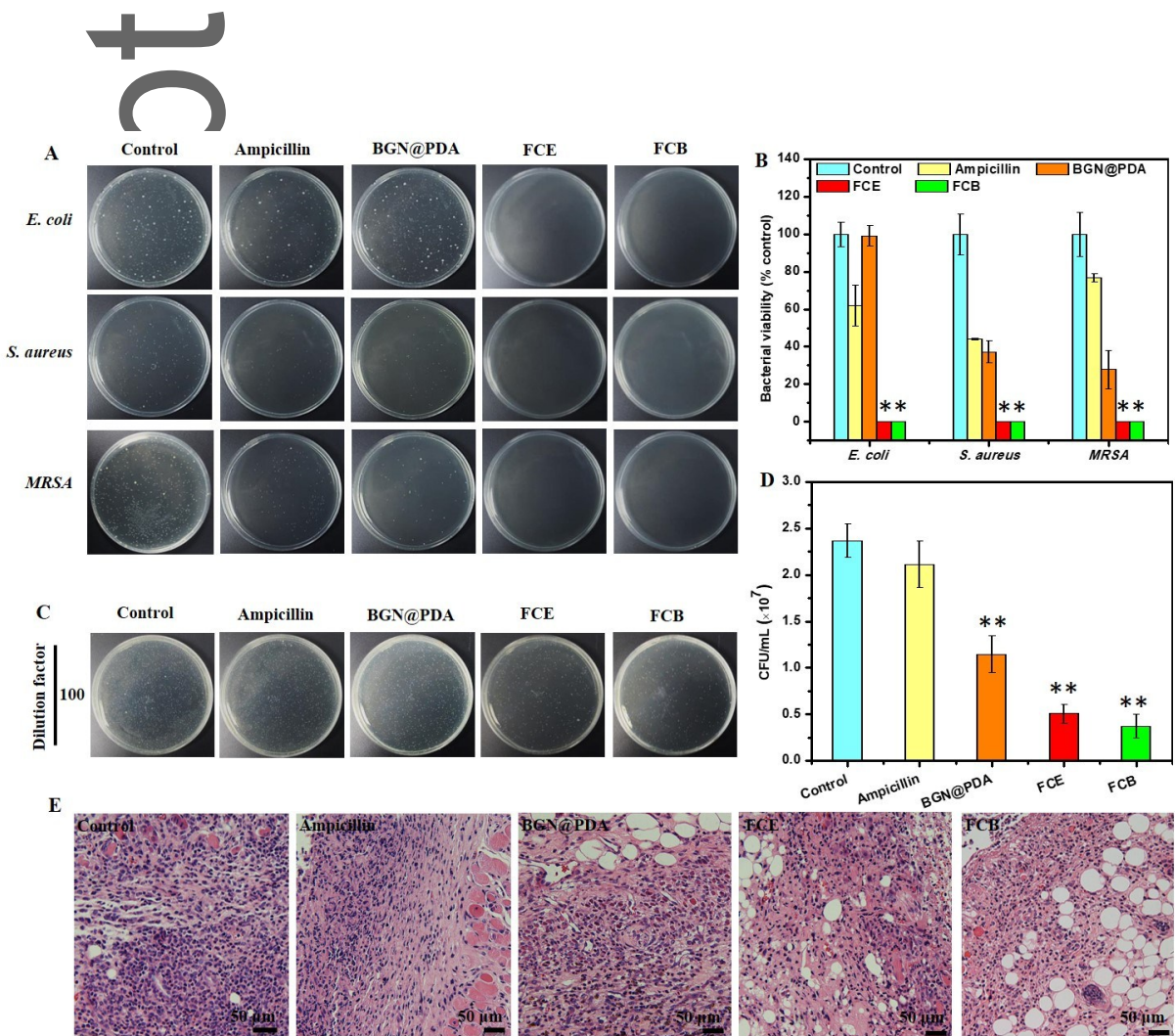


Figure 5

Autho

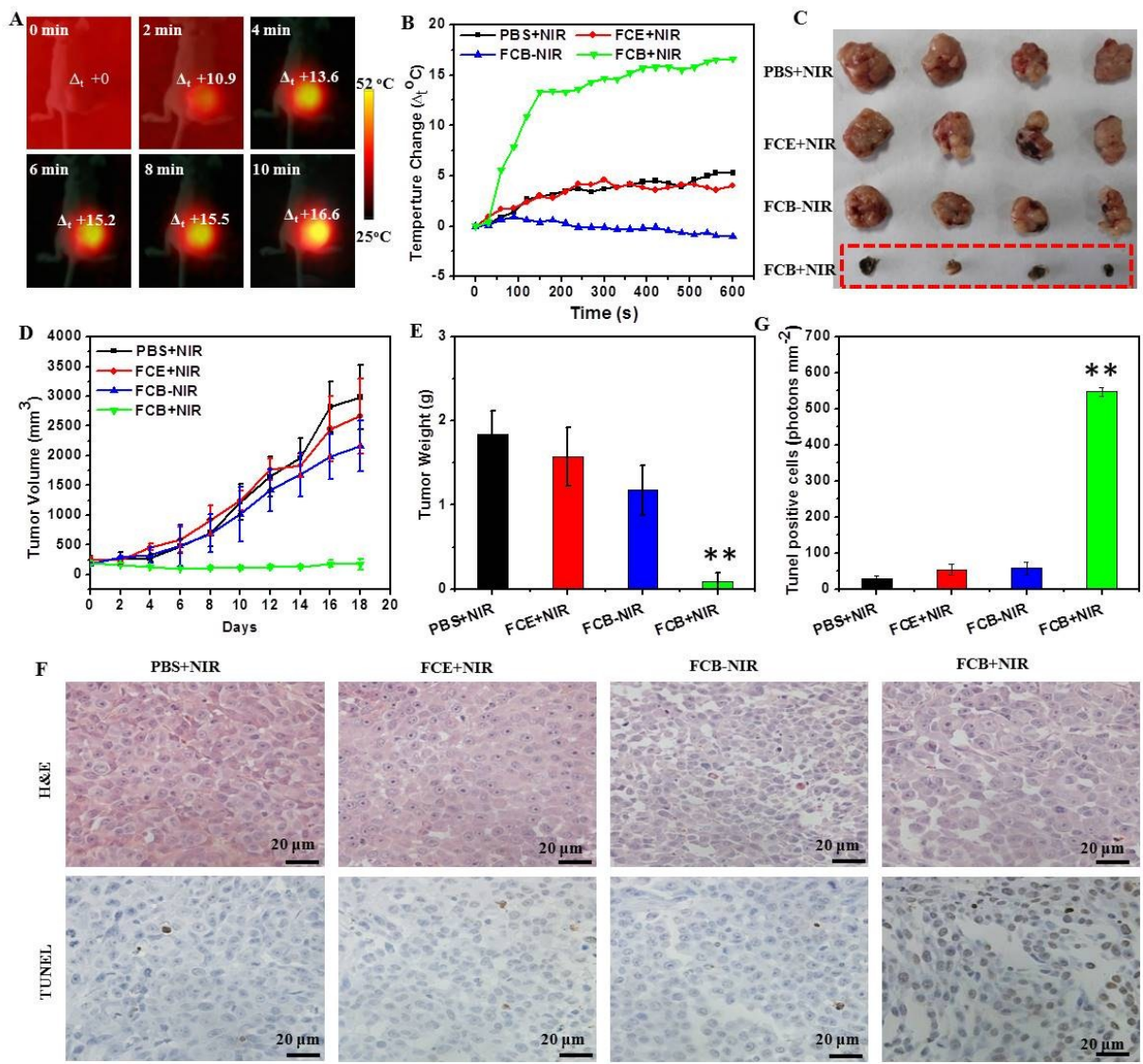


Figure 6

Author

ot

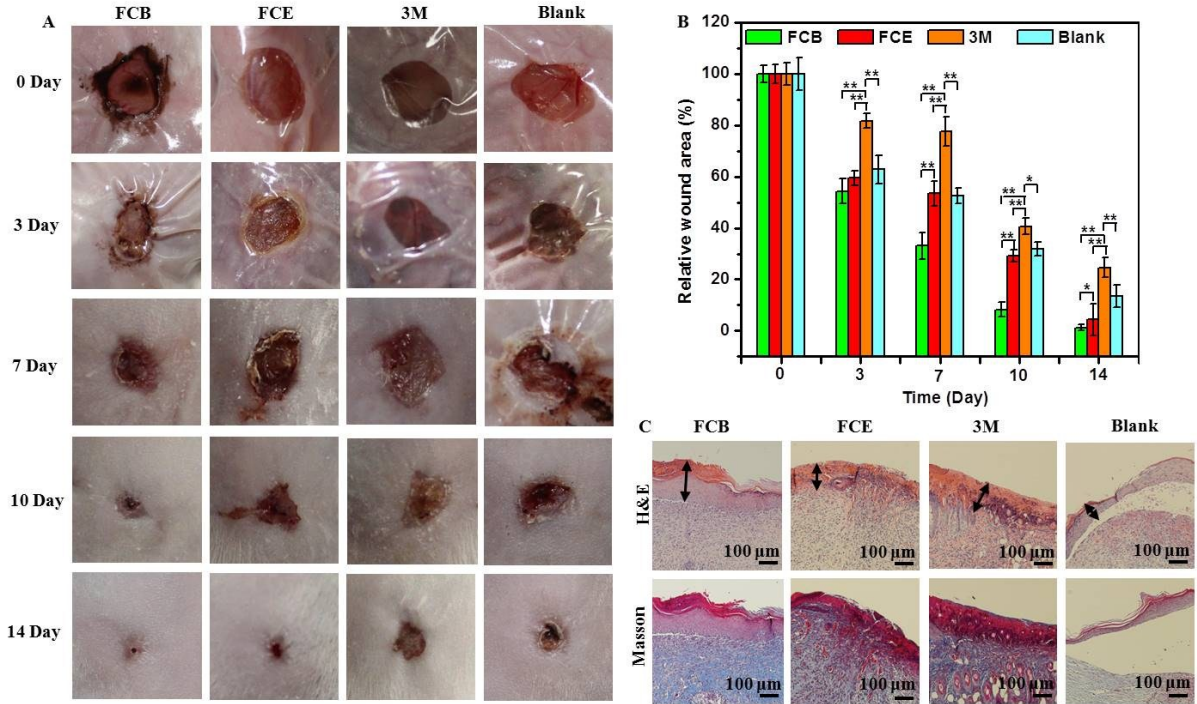


Figure 7

Author N